Journal of Constructional Steel Research 184 (2021) 106803

Contents lists available at ScienceDirect

Journal of Constructional Steel Research

Non-linear analysis models for Composite Plate Shear Walls-Concrete Filled (C-PSW/CF)

Emre Kizilarslan [a,*], Morgan Broberg [b], Soheil Shafaei [b], Amit H. Varma [b], Michel Bruneau [a]

[a] Dept. of Civil Structural and Environmental Engineering, University at Buffalo, Buffalo, NY 14260, United States of America
[b] Lyles School of Civil Engineering, Purdue University, West Lafayette, IN 47907, United States of America

ARTICLE INFO

Article history:
Received 2 November 2020
Received in revised form 10 May 2021
Accepted 10 June 2021
Available online 3 July 2021

Keywords:
Composite plate shear walls
Nonlinear modeling
Flexural behavior
Ductility
Strength degradation

ABSTRACT

Composite Plate Shear Walls-Concrete Filled (C-PSW/CF) are a special seismic-force resisting system consisting of steel plates and concrete infill. Composite walls have been occasionally built in the past decades, but their use for seismic application is fairly new and particularly attractive. As a result, there is a need (by researchers as well as practicing engineers) for nonlinear inelastic hysteretic models that can be used in pushover analyses, cyclic analyses, and seismic response analysis of C-PSW/CF and coupled C-PSW/CF. This paper describes two different approaches for modeling C-PSW/CF walls for these purposes. In a first approach, walls are modelled using a fiber-hinge elements (i.e., distributed plasticity model) using model with constitutive equations that account for both buckling and fracture of the steel. In the second approach, the walls are modelled with fiber-hinge elements having effective stress-strain curves derived from results of 3D finite element analyses.

1. Introduction

Composite Plate Shear Walls-Concrete Filled (C-PSW/CF) are special seismic-force resisting system consisting of steel plates and concrete infill. In essence, C-PSW/CF are "sandwich walls" made of two steel plates with concrete infill in between them. The steel plates are connected to each other using through-thickness tie bars. The steel plates serve as the primary reinforcement for the concrete infill and provide stay-in-place formwork during construction. The concrete infill also prevents inward local buckling of the steel plates thus improving their stability [1,2,26]. Although the structural system has existed for decades [3,4], its use in seismic applications is new [5–7]. At the time of this writing, ASCE-7 and AISC-341 are in the process of balloting provisions for coupled C-PSW/CF, to be designed with a seismic force reduction factor of 8 and in accordance with capacity design principles [8,9], on the basis of findings from a recent FEMA P-695 study [10,11].

Due to its relative novelty in seismic regions, it is foreseeable that C-PSW/CF (and coupled C-PSW/CF) will be the subject of much research in upcoming years, relying on non-linear inelastic analyses. Also, for large projects, implementations in severe seismic regions will often entail design verification at the Maximum Considered Earthquake (MCE) level, which may also require performing non-linear inelastic analyses. As for any structural system, accurate nonlinear inelastic hysteretic models are required to best predict the pushover, cyclic, and seismic response of C-PSW/CF. A large number of such models exists, but to be useful, their application to specific structural systems requires that the numerical values for many of their parameters be calibrated to existing experimental results. Their effectiveness in replicating the physically observed hysteretic behavior must also be qualitatively assessed.

This paper presents two different approaches to model C-PSW/CF for this purpose. In the first approach, walls are modelled using a fiber-hinge element (i.e., distributed plasticity model) using model with constitutive equations that account for both buckling and fracturing of the steel, developed by Kunnath et al. [12]. In the second approach, the walls are modelled with fiber-hinge elements having effective stress-strain curve obtained from results of 3D finite element analysis. The research presented here describes how these models were calibrated using two sets of tests for different wall configurations (planar and C-shaped walls). The resulting calibrated models are provided for the benefit of others, either to use as-is in immediate applications, or as a basis to further improve upon in future research.

2. Material models

Finite element analyses based on continuum mechanics using fine meshes and three-dimensional material constitutive relationships can be helpful for research purposes focusing on individual composite structural members and moderate size assemblies, but their level of complexity and extensive CPU-time requirements makes their use still prohibitive in many other applications. As such, for the non-linear inelastic analysis of complete composite structures subjected to seismic

* Corresponding author.
E-mail addresses: emrekizi@buffalo.edu (E. Kizilarslan), mbroberg@purdue.edu (M. Broberg), sshafaei@purdue.edu (S. Shafaei), ahvarma@purdue.edu (A.H. Varma), bruneau@buffalo.edu (M. Bruneau).

https://doi.org/10.1016/j.jcsr.2021.106803
0143-974X/

excitation, structural analysis models relying on inelastic macro (for example, plastic hinge) models are more effective and thus more commonly used. Here, the software OpenSees [13] has been selected as it is a widely used open-source platform that allows to model nonlinear behavior using discrete plastic hinge or distributed fiber hinge models, with relatively rapid execution time compared to other software platforms. Moreover, OpenSees provides a wide range of constitutive models, elements, and solution algorithms. Hundreds of researchers have been using OpenSees for nonlinear earthquake analysis, for various purposes, including to conduct Incremental Dynamic Analysis (IDA), e.g., [10,11,14–16] of the type required within the framework of FEMA P695 studies [17].

From the extensive list of material models available in the OpenSees library, the *Reinforcing Steel Material* and *Concrete02* models were chosen for the steel and concrete parts of C-PSW/CF, as they were deemed best able to replicate the key behaviors germane to this type of composite walls – particularly with respect to the steel plates behavior. The *Reinforcing Steel Material* model was developed by Kunnath et al. [12]. The advantage of this particular material model is that its constitutive equations allow simulating both buckling and fracture. The ability to model steel fracture and the ensuing loss of cross-section strength is primordial given that past experiments have shown that it is fracture (and not local buckling) that leads to strength degradation in composite walls. The *Reinforced Steel Material* is currently the only OpenSees material model capable of accounting for steel fracture. It is based on the Chang and Mander [18] uniaxial material, available in OpenSees, but with the added benefit of being able to model fracture by eliminating the strength and stiffness of a fiber once it has reached specified cumulative plastic strains. Even though the material was originally calibrated to model reinforcing steels, input parameters can be set to represent the behavior of construction steel in a general sense. The model requires to input the following parameters: yield stress in tension, f_y, ultimate stress in tension, f_u, initial elastic Young's modulus, E_s, tangent at the initial strain hardening, E_{sh}, strain corresponding to initial strain hardening, ε_{sh}, strain at peak stress, ε_u for defining stress-strain curve; slenderness ratio, L_{sr}, amplification factor for the buckled curve, β, buckling reduction factor, r, buckling constant, γ for buckling; the ductility constant, C_f, cyclic strength reduction constant, C_d, the Coffin-Mason Constant, α, for the Coffin-Manson fatigue fracture model; hardening constant, *a1* (default =4.3), limit for the reduction of the yield plateau, limit (default = 0.01) for the isotropic hardening; and three constants, *R1* (default = 0.333), *R2* (default = 18) and *R3* (default = 4), for Menegotto and Pinto Curve parameters.

The *Concrete02* material model in OpenSees was used for concrete fibers. The model is based on the work of Hisham and Yassin [19] and uses Modified Kent-Park model equations. The model simulates concrete damage by stiffness degradation when unloading/reloading excursions occur at increasing strain. However, the model does not capture the possible reduction of concrete strength in subsequent excursions at a given strain. The model allows accounting for tension stiffening, which is the ability of concrete to resist tensile stress between cracks, providing additional flexural stiffness. As magnitude of tension stresses increases, more cracks form, reducing the ability to provide tensile stiffness to the concrete. The *Concrete02* model accounts for this phenomenon using a linear reduction of tensile strength after fracture strength of concrete is reached. It is a more commonly used model that requires seven parameters: the concrete compressive strength at 28 days, f_{pc}, concrete strain at maximum strength, ε_{co}, concrete crushing strength, f_{pcu}, concrete strain at crushing strength, ε_{cu}, ratio between unloading slope at ε_{cu} and initial slope, *lambda*, tensile strength, f_t, and tension softening stiffness, E_{ts}.

The concrete inside composite walls is confined to some degree, especially by the steel closure plates at the ends of the walls. The uniaxial stress-strain model for confined concrete in steel tubes developed by Susantha et al. [20] was used here to determine the values for the parameters of the *Concrete02* material model in OpenSees. Note that the Susantha et al. model was originally developed analytically and verified against existing experimental results for concrete-filled steel tube columns. The Susantha et al. stress-strain relationships were developed by modifying a prior model by Chang and Mander [18], such that:

$$f_c = f'_{cc} * \frac{x * r}{r - 1 + x^r} \tag{1}$$

$$x = \frac{\epsilon}{\epsilon_{cc}} \tag{2}$$

$$r = \frac{E_c}{\left(E_c - \frac{f'_{cc}}{\epsilon_{cc}}\right)} \tag{3}$$

$$\epsilon_{cc} = \epsilon_c * \left[1 + 5 * \left(\frac{f'_{cc}}{f'_c} - 1\right)\right] \tag{4}$$

where f'_{cc} is the maximum confined concrete strength; and ε_{cc} is the strain at peak of confined concrete strength and $\alpha f'_c$ is the residual strength of the confined concrete. Note that the initial slope for this model is calculated by $2^* f_{pc}/\varepsilon_{cc}$. The initial slope calculated within the code of *Concrete02* material model using confined concrete parameters by Susantha et al. stress-strain relationships gives less stiffness. Therefore, here, the strain at maximum strength was calculated by $\epsilon_{cc} = 2 * \frac{f_{pc}}{E_c}$ such that the initial stiffness slope matched with the predicted stiffness per the ACI equation (provided in Section 19.2.2 of ACI-318 [21]); note that there was a 10% difference in the strains calculated by the two equations. In this model, the expression for maximum confined concrete strength is given by:

$$f'_{cc} = f'_c + m * f_{rp} \tag{5}$$

where f_{rp} is the maximum radial pressure on concrete and m is an empirical coefficient. Note that the equations for f_{rp} must recognize that in CFT, concrete and steel expand together. Also, for Eq. (5), Susantha et al. suggested to apply a 0.85 constant reduction for f'_c in the calculation for f'_{cc}. Based on experiments, m value was found to be in the range of 4–6. The authors recommended 4.0 for the m parameter. The radial pressure is given by:

$$f_{rp} = \beta \frac{2 * t}{D - 2 * t} * f_{sr} \tag{6}$$

$$\beta = \nu_e - \nu_s \tag{7}$$

$$\nu_e = 0.2312 + 0.3582 * \nu'_e - 0.1524 * \frac{f'_c}{f_y} + 4.843 * \nu'_e * \frac{f'_c}{f_y} - 9.169 * \left[\frac{f'_c}{f_y}\right]^2 \tag{8}$$

$$\nu_e = 0.881 x 10^{-6} * \left(\frac{D}{t}\right)^3 - 2.58 x 10^{-4} * \left(\frac{D}{t}\right)^2 + 1.953 x 10^{-2} * \left(\frac{D}{t}\right) + 0.4011 \tag{9}$$

where f_{sr} is the circumference stress in steel, t is the thickness, D is taken as the equivalent diameter (D_{eq}) for box sections defined by Eq. (10), and ν_e and ν_s is the Poisson ratios of a steel tube with and without filled-in concrete, and where ν_s is taken as 0.5 at the maximum strength point (0.5 being the Poisson's ratio of steel in a fully plastic state).

$$D_{eq} = \frac{2 * b}{\sqrt{\pi}} \tag{10}$$

The ductility increases if steel restrains concrete in the lateral direction. The restraining action depends on both the material properties and geometry of the column. Therefore, the stress-strain behavior post peak-stress should account for these factors. Beyond the point of maximum strength, the model decreases strength using a linear relationship based on experimental curve fitting and given by:

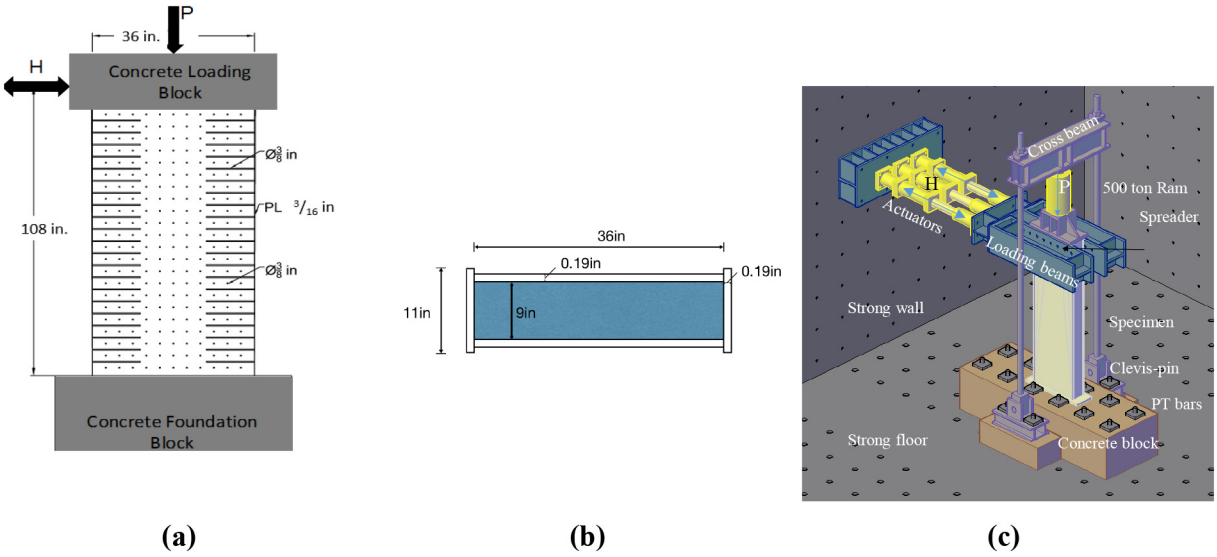

Fig. 1. C-PSW/CF walls in (a) elevation view and (b) plan view and (c) total test setup (Note: 1 in. = 25.4 mm).

$$Z = \begin{cases} 0 & R_t * \frac{f'_{rc}}{f_{yst}} \le 0.0039 \\ \left[23400 * R_t * \frac{f'_c}{f_y} - 91.26\right] MPa & R_t * \frac{f'_{rc}}{f_{yst}} > 0.0039 \end{cases} \quad (11)$$

$$\varepsilon_{cu} = \begin{cases} 0.04 & R_t * \frac{f'_{rc}}{f_{yst}} \le 0.042 \\ 14.50\left(R_t * \frac{f'_c}{f_y}\right)^2 - 2.4 * R_t * \frac{f'_c}{f_y} + 0.116 & 0.042 < R_t * \frac{f'_{rc}}{f_{yst}} < 0.073 \\ 0.018 & R_t * \frac{f'_{rc}}{f_{yst}} \ge 0.073 \end{cases} \quad (12)$$

where f'_{rc} is the reduced unconfined compressive strength of concrete calculated as $0.85^* f'_c$ per Susantha et al. [20], f_{yst} is the yield strength of steel and R_t is the radius-to-thickness ratio parameter is given by Eq. (13).

$$R_t = \sqrt{3*(1-\nu^2)} * \frac{f_y}{E_s} * \frac{D}{2*t} \le 0.125 \quad (13)$$

where ν is the Poisson's ratio.

The slope of the descending branch increases as $R_t f'_c / f_{yst}$ increases. Once the slope is determined, the coefficient for residual strength can be calculated from following expression:

$$\alpha = 1 - \frac{Z}{f'_{cc}}(\varepsilon_{cu} - \varepsilon_{cc}) \quad (14)$$

Table 1
Concrete inputs for planar C-PSW/CF walls (Note: 1 ksi = 6.9 MPa).

Specimens	E_C, ksi	Region 1			Region 2			Z, ksi
		f_{pc}, ksi	ε_{co}	f_{cu}, ksi	f_{pc}, ksi	ε_{co}	f_{cu}, ksi	
CW-42-55-10-T	4598	8.60	3.75E-3	7.79	6.50	2.83E-3	5.88	25
CW-42-55-20-T	5031	9.75	3.88E-3	8.67	7.79	3.10E-3	6.92	33
CW-42-14-20-T	5329	10.77	4.04E-3	9.50	8.74	3.28E-3	7.70	38
CW-42-14-20-TS	5227	10.42	3.98E-3	9.21	8.41	3.22E-3	7.43	36
CW-42-55-30-T	4899	9.31	3.80E-3	8.31	7.39	3.02E-3	6.59	30

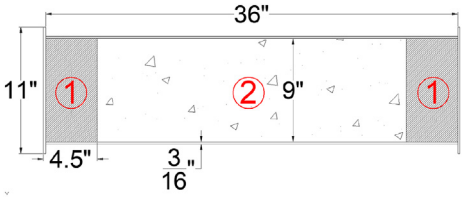

Fig. 2. Two different concrete regions where different properties were assigned to the cross-section (Note: 1 in. = 25.4 mm).

where Z is the descending linear slope after peak strength calculated by Eq. (11).

3. Element type

The material elements described before are used in cross-sections that themselves are part of element of given length for which plastic hinge rotations can be obtained. Building model with 3D element might give more accurate results in terms of global and local responses but it would be substantially more computationally expensive to perform nonlinear inelastic analysis. Therefore, 2D beam element types

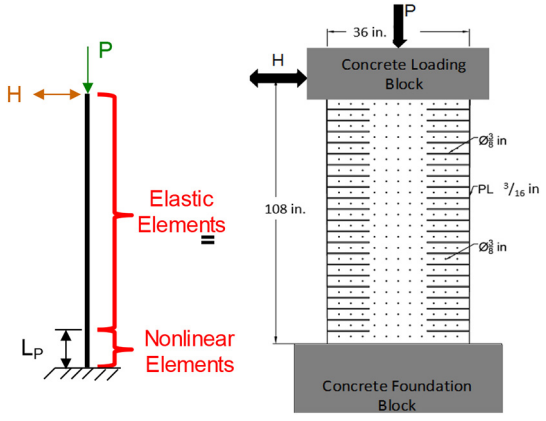

Fig. 3. Representation of OpenSees models for the wall specimens (Note: 1 in. = 25.4 mm).

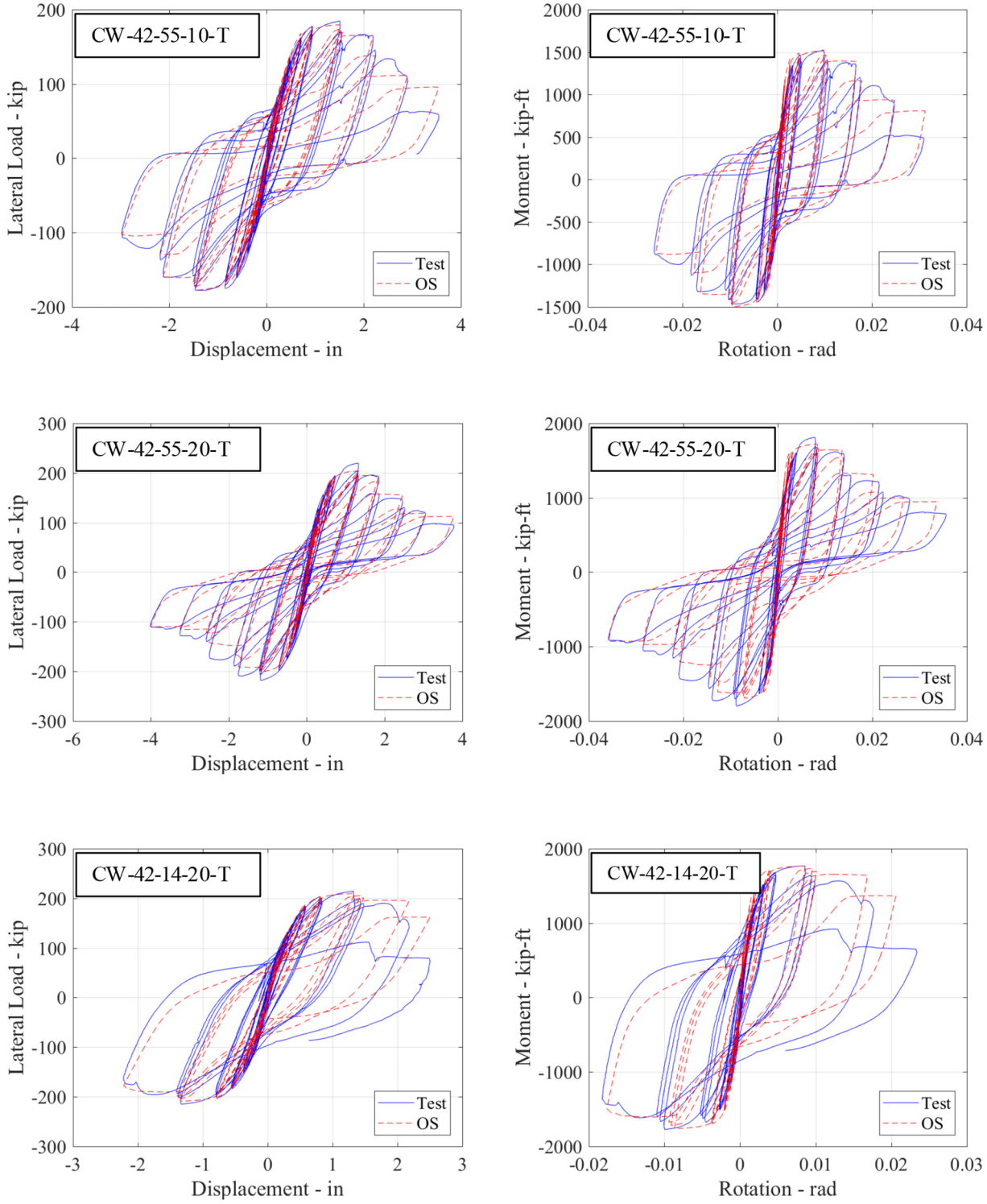

Fig. 4. Base shear-displacement (left) and moment-rotation (right) comparisons of OpenSees models with test data (Note: 1 in. = 25.4 mm; 1 kip = 4.45 kN).

were selected here to describe the hysteretic behavior while achieving manageable computational times. Furthermore, for the purpose of calibrating the non-linear inelastic models against experimental results for walls and coupling beams, plastic hinge locations and lengths were determined, nonlinear elements were only assigned to these locations, and the non-yielding parts of the wall were modelled using elastic beam column elements. Due to space constraints here, details on the determination of plastic lengths are provided in Bruneau et al. [10] and Kizilarslan et al. [11].

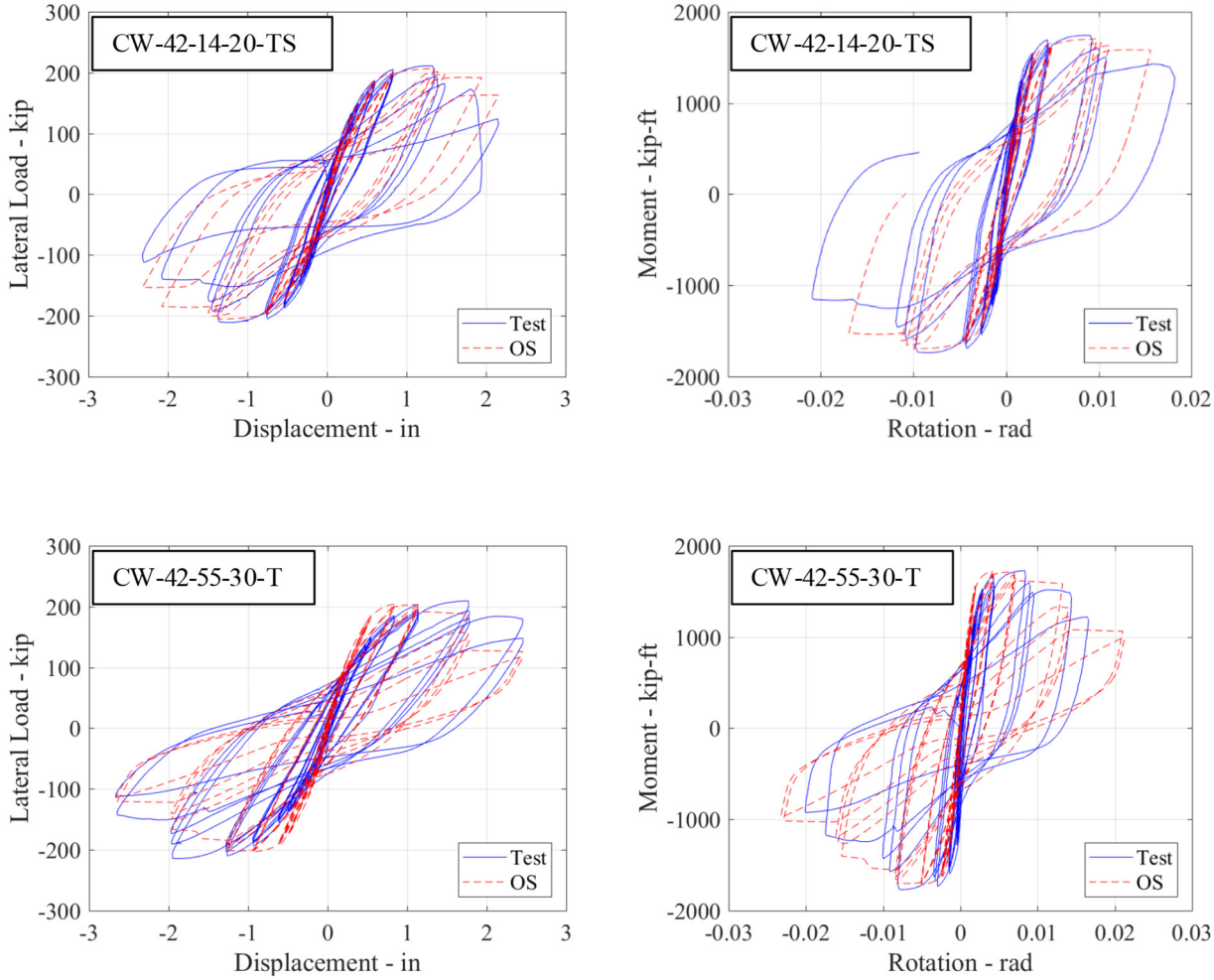

Fig. 4 (*continued*).

There are two types of nonlinear elements in OpenSees, namely force-based (a.k.a flexibility-based) and displacement-based (a.k.a. stiffness-based) elements. Examples of two options for force-based elements are "beamWithHinge" and "nonlinearBeamColumn" elements; and the "dispBeamColumn" is the only displacement-based element. Both type of elements allows spread of plasticity along elements. The modeling of these two types of elements, however, is performed differently to obtain a comparable level of accuracy. Fundamentally, both types of elements require an iterative process for solving, and the main difference is that displacement-based methods iterate from an initial displacements of nodes, while the force-based methods iterate from an initial set of nodal forces. For the purpose of convergence in earthquake analysis, displacement-based elements were preferred in simulating wall elements. To increase accuracy, sufficient nonlinear elements were used in the plastic hinge region.

4. Modeling

Calibration was performed for the two different modeling approaches adopted for nonlinear inelastic analysis. In the first approach, walls were modelled using a fiber-hinge elements (i.e., distributed plasticity model) and the *Reinforcing Steel Material* model described above that account for both buckling and fracturing of the steel [12]. In the second approach, the walls were modelled with fiber-hinge elements having effective stress-strain curve obtained from the results of 3D finite element analyses. In all cases, properties obtained from coupon test results and unconfined concrete strength for each experiments were used. Two different set of test results were used for the calibrations to address both planar and C-shaped walls.

4.1. Calibration for planar C-PSW/CF

Five planar C-PSW/CF walls tested by Shafaei et al. [22,23] were used for calibrating the models on planar walls. In this test series, both axial and cyclic loading were applied at the top of the specimens with a 500-ton actuator connected through a loading frame pinned at its base; lateral load was applied to the specimen using horizontal actuators. The elevation view, cross-section of walls and test set-up is shown in Fig. 1(a), (b), and (c), respectively. The height-to-length ratio (H/L) of the specimens is 3.0 and the specimens were subjected to constant axial forces equal to either 10%, 20%, or 30% of the strength of the concrete area (i.e., $A_c f'_c$). Specimens also had one of three different tie reinforcement ratios (namely, 0.14%, 0.24%, and 0.55%), where this ratio is defined as the area of the tie bar divided by the spacing between tie bars, squared. Note that the specimens were named based on their properties. For example, the CW-42-55-10-T specimen had a 4.2% reinforcement ratio (which is defined as the percentage of the total gross cross section area taken by the area of the steel plates), 0.55% tie bar reinforcement ratio, was subjected to an axial load equal to 10% of concrete crushing strength, and only had tie bars ("T" – whereas "TS" was used when tie bars (T) and shear studs (S) were combined in alternate rows. More specifically this case, tie bars were spaced at 9 *in.* (228.6

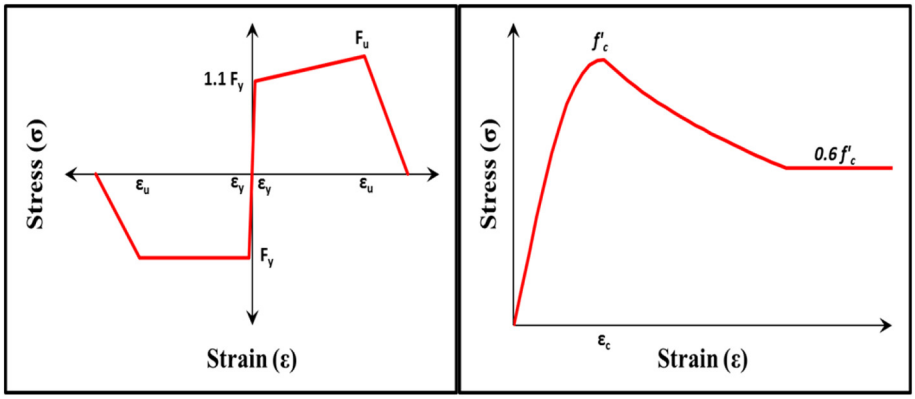

Fig. 5. Effective Stress-strain curves for (a) steel and (b) concrete behavior [22,23].

mm) and between the two rows of ties, a row of shear studs was added (both in the vertical and horizontal directions). The resulting spacing was 4.5 *in.* (114.3 *mm*) and corresponding plate slenderness 4.5/(3/16)). More details regarding the specimens can be found in Shafaei et al. [22,23].

4.1.1. Distributed plasticity model (DPM) approach

The same buckling and low-fatigue parameters were assigned to the *Reinforcing Steel Material* used for all steel plates. Also, the concrete confinement model by Susantha et al. [20] was used to determine the concrete strength and ductility at both ends of the cross-section over a length equal to half the width of the cross-section, while rest of the concrete cross-section was assigned a concrete model having unconfined concrete strength (corresponding to the value measured on the day of the testing) but with the same ductility as that of the confined concrete.

The backbone curves of the steel material were defined by the parameters, f_y, E_s, ε_y, f_u, E_{sh}, ε_{sh}, and ε_u to replicate the data from coupon test, using values of 61.2*ksi* (422 *MPa*), 22500*ksi* (*155GPa*), 0.00211, 68.6*ksi* (473 *MPa*), 1125*ksi* (7757 *MPa*), 0.00221 and 0.15. For the five planar C-PSW/CF walls tested used for calibration of the hysteretic steel model, different axial loads and tie spacing were used (as mentioned previously), and, correspondingly, buckling and fracture occurred at different points along the hysteretic response history, but at similar locations on the wall. However, the calibration objective was to replicate as closely as possible the five planar walls test results with a single set of buckling and fracture parameters, to be used generally in nonlinear inelastic analysis. After many trials, good results were empirically obtained for the buckling parameters using a buckling curve reduction factor, *r*, of 0.4; an amplification factor, β, of 1.0; and a buckling constant, γ, of 1.0 for buckling. Slenderness ratio is defined as the unsupported length (the length between tie bars in this system) divided by the thickness of the steel plate. Since the slenderness ratio in this model is a physical parameter (i.e. the ratio changes based on the unsupported length), different slenderness ratios were used for walls having 4.5 *in.* (114 *mm*) tie spacing (20.8) and 9 *in.* (229 *mm*) tie spacing (41.6), which was calculated by dividing the tie spacing by the equivalent bar diameter (equating the radius of gyration of a bar having $d_{b,eff}$ to the radius of gyration of the rectangular steel plate of the composite walls). As for the low cycle fatigue parameters, using a fatigue ductility coefficient, C_f, of 0.21, a fatigue ductility exponent, α, of 0.515, and a cyclic strength reduction constant, C_d, of 0.3 allowed to replicate closely the observed hysteretic behavior of the tested specimens, including the strength and stiffness degradation observed in repeated excursions at the same drift. Default values for the Menegotto-Pinto curve parameters and hardening constant were used (see above). As for the concrete, based on the findings of Susantha et al. [20] study, it was judged appropriate here to model the ends of the walls are confined differently than the rest of the cross-section. The length of the confinement at the ends were chosen as half of the width of the specimens, following an approach similar to how Susantha et al. [20] came up with the parameters for confined behavior of concrete inside concrete-filled steel tubes of rectangular cross-section. The values for the confined concrete parameters were obtained by entering measured average concrete strength from cylinder tests into the Susantha et al. [20] equations for rectangular composite cross-section at the ends of the concrete cross-section (Table 1). The same ε_{cu}, α, and *Lambda* values are used for all specimens, which are 0.04, 0.7, and 0.9, respectively. In addition, the same ductile behavior was given to the concrete located between these ends (Region 2 in Fig. 2), but using the average unconfined concrete strength from cylinder tests.

Displacement-based nonlinear elements were only assigned to the plastic hinge region of the walls and elastic elements were used for the rest of the wall specimens (Fig. 3). The plastic hinge length was again determined from the vertical distance between the yield (1063*kip-ft* (1441*kN-m*)) and plastic (1115*kip-ft* (1512*kN-m*)) moments of the cross-section. This resulted in a 5.04 *in.* (128 *mm*) plastic hinge length, but this length was increased to 18 *in.* (457 *mm*), to include two more 6 *in.* (152 *mm*) elements to account for the fact that the maximum moment developed at the base can be greater than the plastic moment value.

Base shear versus displacement (or lateral load-displacement) are plotted on the left side of Fig. 4a to e; corresponding moment-rotation hysteretic curves are plotted on the right side of these figures.

Table 2
Steel material properties used for planar wall benchmarking (Note: 1 ksi = 6.9 MPa).

Parameter	Value	Parameter	Value
E_s (ksi)	29,000	L_{sr}	10
b	0.01	*beta*	1
E_{sh} (ksi)	290	*r*	0.65
F_y (ksi)	59.1	*gamma*	0.5
F_u (ksi)	68.5	C_f	0.6
ε_{sh}	$2*F_y/E_s$	*alpha*	0.5
ε_{ult}	0.1	C_d	0.35

Table 3
Concrete material parameters for planar wall benchmarking (Note: 1 ksi = 6.9 MPa).

	SP1	SP2	SP3	SP4	SP5
f'_c (ksi)	6.5	7.8	8.7	8.4	7.4
e_{psc0}	0.0023	0.0025	0.0026	0.0026	0.0024
F_{pcu} (ksi)	3.9	4.7	5.3	5.1	4.4
e_{psu}	0.0071	0.0071	0.0071	0.0071	0.0071
E_{ts} (ksi)	4566	4996	5292	5190	4865

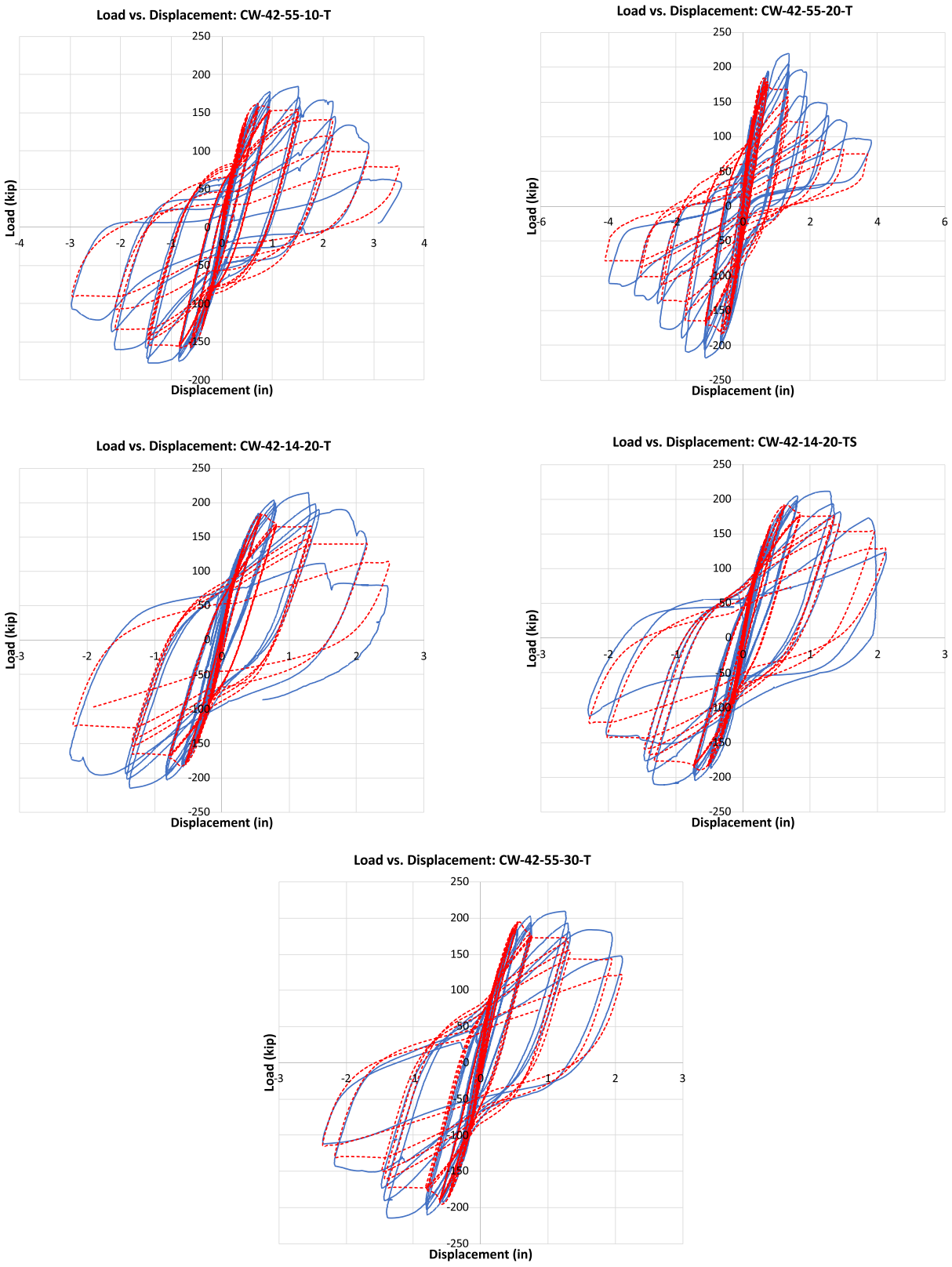

Fig. 6. Load vs. Displacement benchmarking results for planar wall experiments.

Displacements and base rotations were obtained from linear potentiometers and inclinometers, respectively. Moments were obtained by multiplying the values of the lateral load at the top of the wall (equal to base shear values) by the distance from the top of wall to the location where the inclinometers (107.25 *in.* (2724 *mm*)) were placed for calculating rotation.

Results obtained from the OpenSees model of the *CW-42-55-10-T* specimen closely matched the experimental data, with small errors, as

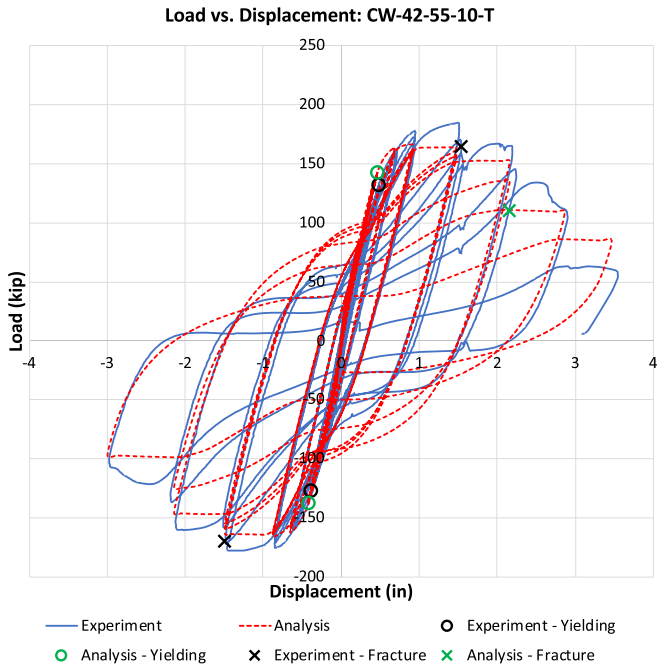

Fig. 7. Load vs. Displacement benchmarking results considering specific effective steel and concrete properties for CW-42-55-10-T (Note: 1 in. = 25.4 mm; 1kip = 4.45 kN).

shown in Fig. 4a. The maximum force of 185*kips* (823*kN*) (hence maximum moment of 1523*kip-ft.* (2065*kN-m*)) was matched within 2.7%. In addition, the rotation at maximum force (0.00982 *rad*), corresponding to when the specimen was displaced 1.50 *in.* (38.1 *mm*), matched with a maximum difference of 13%. The difference in maximum lateral load increased to 7% for the *CW-42-55-20-T* specimen. However, in the first excursion at 2.5 *in.* (63.5 *mm*) displacement in the negative direction, the discrepancy in lateral load increased to 19%, even though a relatively good match (8% difference) was obtained for the same excursion in the positive direction. For the moment-rotation curve comparison, the rotation at maximum moment of 0.0079 *rad*, reached when the drift was 1.33 *in.* (33.8 *mm*) matched with a maximum difference of 18%. By comparison, the maximum lateral load capacity and moment capacity obtained with OpenSees were only within 1.8% of the experimental results for Specimen *CW-42-14-20-T*. Also, the rotation at maximum force matched within 5%. However, the sudden drop in strength that occurred during the last excursion was not captured by the analytical model. The difference in the maximum lateral load (or moment) and rotation are 1.4% and 8% for Specimen *CW-42-14-20-TS*, respectively. However, the last two excursions did not match as closely as for the other specimens, with maximum differences of 30% in lateral load capacity. For the Specimen *CW-42-55-30-T*, the lateral load capacity matched within 10%. For this particular specimen, the initial stiffness did not match closely experimental curve for the lateral load versus displacement curve, but the same initial stiffness matched better for the moment-curvature curve. In addition, in this case, the OpenSees models started fracturing before the test data. Therefore, there is a mismatch for maximum rotation (70% difference), with the OpenSees results being on the conservative side.

Recall that the objective of the above calibration exercise was to determine a single set of fatigue and buckling parameters matching as best as possible all of the test data of planar C-PSW/CF walls, and that could consequently be used in nonlinear inelastic analyses. Evidently, if the objective instead was to find individual sets of buckling and fatigue parameters to best match each of the test data individually, magnitude of the above discrepancies could have been reduced. Moreover, it should be noted that the pinching and progressive strength degradation were replicated well, which was one of the main reasons why the *Reinforcing Steel Material* model was selected.

4.1.2. Distributed plasticity model with effective stress-strain curve from 3D FEM approach

Another approach was developed based on implementing effective stress-strain curves in a fiber-based model. This approach relied on extracting effective stress-strain curves from a robust 3D finite element model and implementing them in OpenSees. This approach was explored because the 2D fiber analysis methods available in OpenSees are inherently unable to directly capture the mechanics of particular aspects of behavior such steel local buckling, multi-axial stress states, or concrete confinement. This approach is presented in detail in Shafaei et al. [22,23], and only summarized here for reference.

The process of developing effective stress-strain curves involved several key steps: (1) developing and benchmarking a 3D finite element model, (2) extracting the forces carried by the steel and concrete elements over the inelastic hinge, (3) calculating the average stresses in the steel and concrete elements and the average strain over the inelastic hinge, (4) estimating the average stress-strain curves for the steel and concrete elements for each specimen, (5) generalizing and developing effective stress-strain curves for the steel and concrete materials of C-PSW/CF, and (6) validating the effective stress-strain curves by implementing them in a 2D finite element model. This process was developed and detailed in Shafaei et al. [22,23]. The effective stress-strain curves developed using this approach are shown in Fig. 5.

The effective stress-strain curve for steel is defined as: (i) elastic-plastic with 10% increase in f_y and linear strain hardening after yielding in tension, and (ii) elastic-perfectly plastic (with no strain hardening) in compression. The 10% increase in f_y in tension is due to the biaxial stress state (longitudinal and transverse tensile stresses) that develops in the steel plates due to confinement offered to the concrete infill. The elastic-perfectly plastic behavior (with no strain hardening) in compression captures the effects of local buckling on reducing the compressive stress capacity of the steel plates. The pre-peak portion of the effective stress-strain curve for concrete was similar to behavior of unconfined concrete with peak stress of f'_c. The post-peak descending branch was similar to the model defined by Tao et al. [24] for confined concrete in rectangular concrete filled tube columns, and residual value was set at $0.6f'_c$. This residual capacity of concrete is retained due to the effect of confinement.

After developing the effective strain curves, these material models were implemented in OpenSees. Similar to the first method, *Reinforcing Steel* was used to model steel components of the walls, and *Concrete02* was used to model concrete components. Properties from material testing were used to define f_y, f_u, and f'_c. The remainder of the backbone curve was defined to follow the effective stress-strain curves.

The steel material curve properties are reported in Table 2. The *Reinforcing Steel* material in OpenSees was unable to model different yield stresses in tension ($1.1f_y$) and compression (f_y). Therefore, the yield stress was conservatively maintained at f_y for both tension and compression. Properties defining the backbone curve including f_y, f_u, E_s, E_{sh}, ε_y, ε_{sh}, and ε_{ult} were selected to follow the effective stress-strain curves. The buckling parameters, L_{sr}, β, and r, were varied until behavior approximating elastic-perfectly plastic in compression was reached. The fatigue parameters, C_f, α, and C_d, were selected based on trial and error to follow the degradation seen across all specimens.

The concrete material curve properties are reported in Table 3. The average cylinder strength was input into the equations defined by Tao et al. [24] to calculate the remaining parameters. The residual capacity specified in this model was altered to $0.6f'_c$, following the effective stress-strain curves. All concrete in the cross-section was modelled using these material parameters.

Similar to the previous approach, displacement-based nonlinear elements were used to model the plastic hinge region and elastic elements were used for the rest of the height. The length of the plastic hinge was 18 in. The length of the plastic hinge was selected based on the extent of

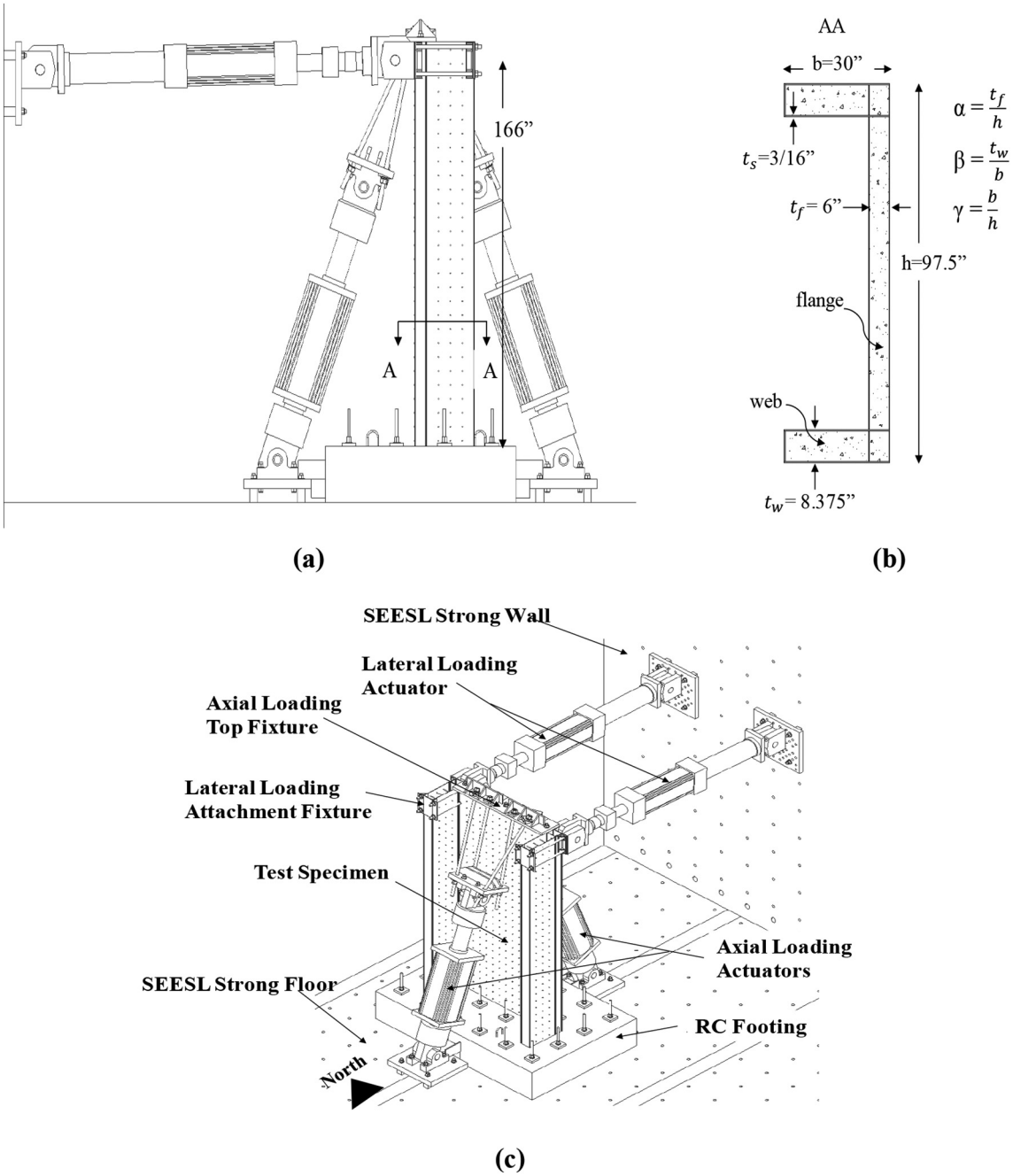

Fig. 8. Details of C-Shaped walls in (a) elevation view and (b) plan view and (c) total test setup (Note: 1 in. = 25.4 mm).

Table 4
Values of concrete parameters for planar C-PSW/CF walls models (Note: 1 ksi = 6.9 MPa).

Specimens	E_C, ksi	Region 1			Region 2			Z, ksi
		f_{pc}, ksi	ε_{co}	f_{cu}, ksi	f_{pc}, ksi	ε_{co}	f_{cu}, ksi	
C1	1819	5.21	5.73E-3	4.66	4.5	4.95E-3	4.02	16
C2	4071	5.88	2.89E-3	5.13	5.1	2.51E-3	4.5	20

yielding seen in the experimental test and 3D finite element analysis. This approach follows the distribution outlined in Fig. 3.

Load versus displacement comparisons for all specimens are plotted in Fig. 6. These curves show a good match between the initial stiffness, load at yield, reloading behavior, and residual capacity. The model is conservative with respect to ultimate strength. This lower ultimate capacity is anticipated because the increase in the yield strength of the steel material in tension, as seen in the effective stress-strain curves, could not be accounted for in these models. These trends hold for all specimens regardless of axial load level, tie spacing, or shear stud spacing.

This comparison can be improved by considering the specific effective stress-strain curves for a specimen. This would make the approach specimen specific and therefore inappropriate for analysis of other geometries. However, the close correlation between the experimental and numerical results suggests the effective stress-strain approach closely correlates to the observed experimental behavior. A comparison for CW-42-55-10-T is shown in Fig. 7. Also noted in Fig. 7 is experimental and analytical milestones, specifically yielding and fracture in the closure plates (a.k.a. flanges) of the planar

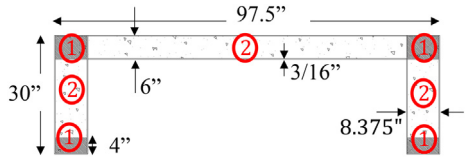

Fig. 9. Regions of the cross-section where different concrete properties were used to model the C-Shaped wall.

walls. For both the push and pull cycles the yielding milestones closely follow each other. Fracture initiates in the experiment before fracture in the fiber model. Although the fiber model does not indicate fracture until two additional cycles, the degradation seen in the fiber model is in good agreement with the experimental data. Additionally, both flanges fracture at nearly the same point in the analytical model. This behavior is inconsistent with the experimental results as plates fractured in tension and buckled in compression. Due to the limitation of a fiber model, the buckling behavior cannot be directly accounted for and the fracture of both flanges initiates during the same push cycle.

4.2. Calibration for C-shaped C-PSW/CF

The calibration of the OpenSees model for C-shaped composite core walls was done using experimental results from the study conducted by Kenarangi et al. [25] at the University at Buffalo on two C-shaped C-PSW/CF (referred as *Specimen C1* and *Specimen C2* from now on) subjected to both axial and cyclic loadings. Fig. 8a to c show the test setup details of the C-shaped wall specimens. The vertical actuators, each with a nominal capacity of 450kips in tension, were used to apply an axial load on the specimen equal to 20% and 15% of $A_g f'_c$ for Specimens C1 and C2, respectively. The cyclic loading was applied by two horizontal actuators, each having a nominal capacity of 220*kips* (979*kN*). Both C-shaped walls cross section had a flange length of 97.5 *in.* (2477 *mm*), web length of 30 *in.* (762 *mm*), and flange thickness of 6 *in.* (152.4 *mm*), as shown in Fig. 8b. For both specimens, the walls were built of 3/16 *in.* (4.8 *mm*) thick steel plates and were 166 *in.* (4216 *mm*) tall. Detailed dimensions, properties of the prototype wall, and properties of the tested specimens can be found at Kenarangi et al. [25].

4.2.1. Distributed plasticity model (DPM) approach

The yield strength (f_y), Young's Modulus (E_s), the ultimate strain (ε_u) and ultimate strength (f_u) (namely, ε_u equal to 0.15 for both specimens and f_u equal to 62.73*ksi* (432.5 *MPa*) and 62.50*ksi* (431 *MPa*) for the *Specimens C1* and *C2*, respectively) were taken from coupon tests. The yield strain (ε_y) was calculated by dividing the yield strength by Young's Modulus. Consistently to what was done before, since a yield plateau was not observed in the stress-strain curves in this case either, the strain at the onset of the strain-hardening strain (ε_{sh}) was set to be 0.0001 greater than the yield strain (ε_y). Also, the strain-hardening Modulus (E_{sh}) was assumed to be 0.01 times the Young's Modulus (E_s). On that basis, a good agreement was observed between the coupon tests and OpenSees results. With respect to wall hysteretic behavior, after many trials, good results were empirically obtained for the buckling parameters using a buckling curve reduction factor, r, of 0.9; an amplification factor, β, of 1.0; and a buckling constant, γ, of 1.0 for buckling. Default values for the Menegotto-Pinto curve parameters and hardening constant were again used. The slenderness ratio, L_{sr}, was calculated by dividing the tie spacing (6 *in.* (152.4 *mm*)) by the equivalent steel plate thickness, which is 20.8. As for the low cycle fatigue parameters, new values were determined to fit the results for the C-Shaped core walls. Using a fatigue ductility coefficient, C_f, of 0.21, a fatigue ductility exponent, α, of 0.575, and a cyclic strength reduction constant, C_d, of 0.4 gave good correlation for the observed hysteretic behavior of the tested specimens, even replicating well the strength and stiffness degradation observed in repeated excursions at the same drift.

The values for the confined concrete parameters (Table 4) were obtained by entering measured average concrete strength from cylinder tests into the Susantha et al. [20] equations for rectangular composite cross section at the ends of the webs, and the corners of flange and webs in the cross-section (Fig. 9). The same ε_{cu}, α, and *Lambda* values are used for all specimens, which are 0.04, 0.1, and 0.9, respectively. In addition, the same ductile behavior was given to the concrete located between the end of webs and corners, but using the average unconfined concrete strength from cylinder tests. Note that Young's modulus of the wall's infill concrete for the *Specimen C1* was measured from linear potentiometers that were attached to the cylinders during the concrete compression tests. This is because the test for *Specimen C1* was conducted only five days after the wall's infill concrete was poured (for reasons presented in Kenarangi et al. [25]). Since concrete was not cured for 28 days, the equation in Section 19.2.2 of ACI-318 [21] was deemed to be not applicable. However, this was not the case for *Specimen C2*, and

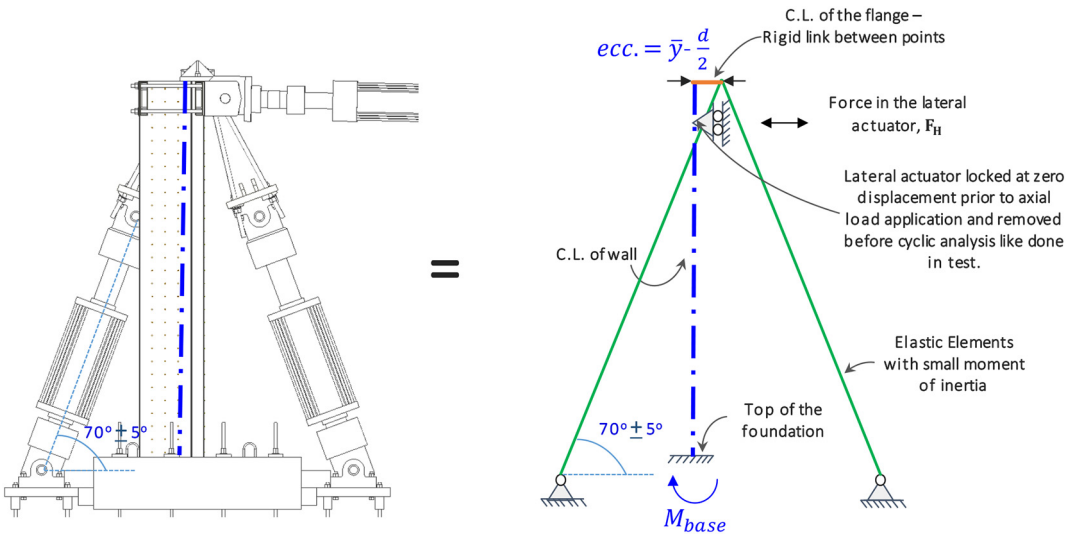

Fig. 10. Representation of OpenSees models for C-Shaped walls.

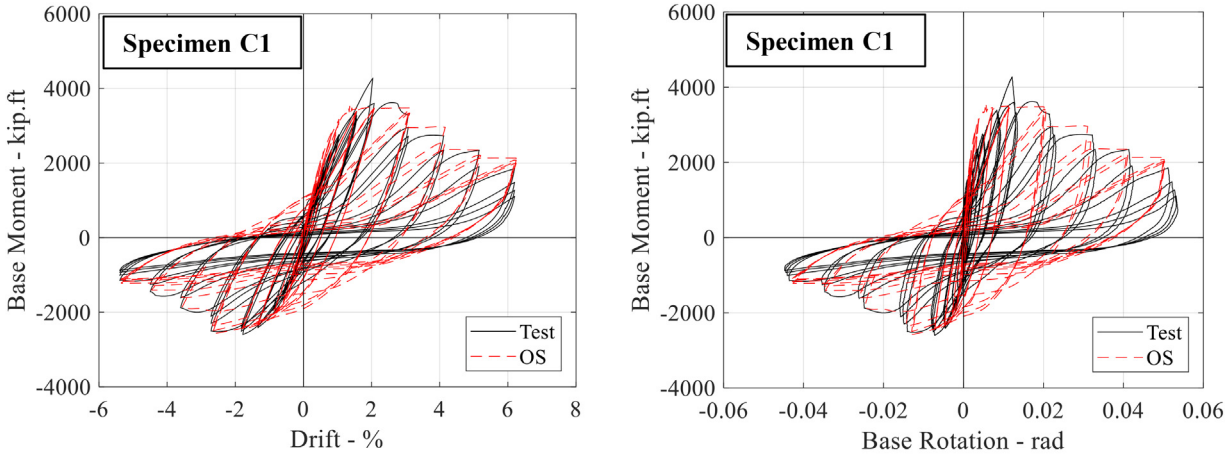

(a)

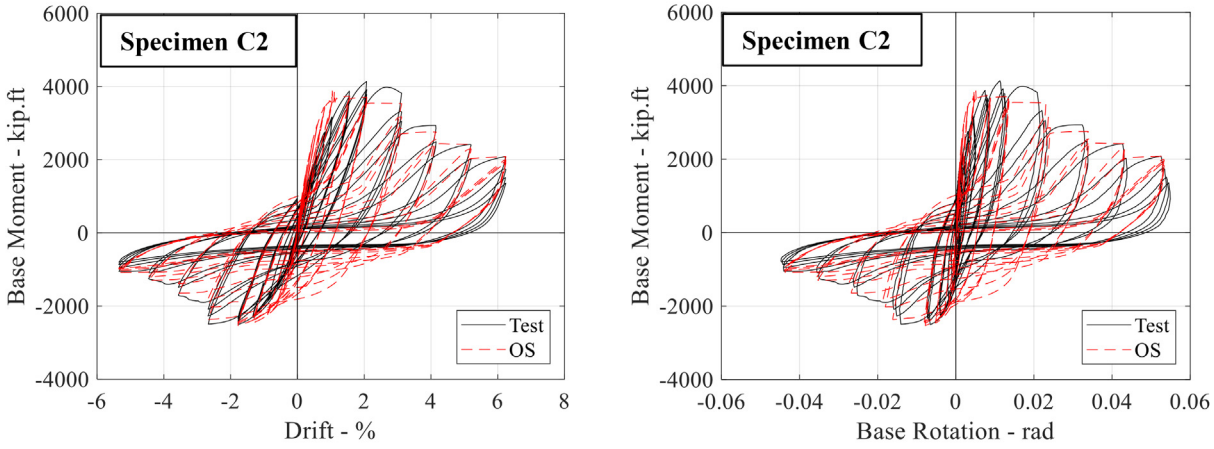

(b)

Fig. 11. Base moment-displacement (left) and base moment-rotation (right) comparisons of OpenSees models with test data (Note: 1 in. = 25.4 mm; 1kip-ft = 1.36 kN-m).

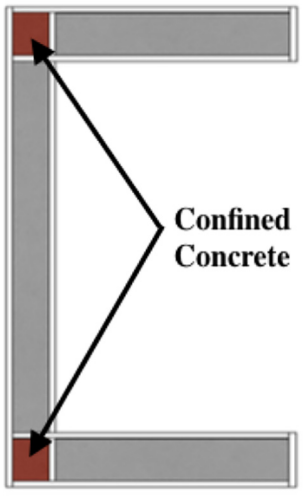

Fig. 12. Schematic depicting locations assigned corner box concrete (concrete with higher residual capacity).

the Young's Modulus in that case was calculated using the equation from ACI-318.

The plastic hinge length was again determined to be the vertical distance between the yield and plastic moments of the cross section (3566*kip-ft.* (4835*kN-m*) in the positive moment direction (i.e., when the web of the cross section is in compression) and 2098*kip-ft.* (2845*kN-m*) in the negative moment direction (i.e., when the flange of the cross section is in compression)). Since the yield and plastic moments differ in the positive and negative directions, the maximum of the two was taken as the plastic hinge length for modeling purposes, which resulted in a 68 *in.* (1727.2 *mm*) plastic hinge length. However, this length was arbitrarily increased to 84 *in.* (2133.6 *mm*), to account for the fact that the plastic hinge length will be longer when considering strain hardening (note that the elements used were 12 *in.* (304.8 *mm*) long).

Fig. 10 shows the test set-up for the C-shaped walls. The moment acting at the base of the wall was calculated with due corrections to account for changes in initial angle between the inclined actuators during cyclic testing, and the small eccentricity from of the point of application of the axial load to the centroid of the section. All these effects were also accounted for, and corrected, in the OpenSees model.

Table 5
Steel material properties used for C-shape wall benchmarking (Note: 1 ksi = 6.9 MPa).

Parameter	Value	Parameter	Value
E_s (ksi)	29,000	L_{sr}	10
b	0.01	beta	1
E_{sh} (ksi)	290	r	0.65
f_y (ksi)	55.4	gamma	0.5
f_u (ksi)	65.0	C_f	0.6
ε_{sh}	$2*F_y/E_s$	alpha	0.5
ε_{ult}	0.1	C_d	0.35

Table 6
Concrete material properties used for C-shape wall benchmarking (Note: 1 ksi = 6.9 MPa).

Material property	Specimen C1		Specimen C2	
	General concrete	Corner box concrete	General concrete	Corner box concrete
f_c' (ksi)	4.5	4.5	5.1	5.1
e_{psc0}	0.0020	0.0020	0.0021	0.0021
f_{cu}' (ksi)	$0.6f_c'$	$1.0f'_c$	$0.6f_c'$	$1.0f_c'$
e_{psu}	0.009	0.009	0.008	0.008
E_{ts} (ksi)	4566	3820	4996	4070

Results obtained from the OpenSees model of the *Specimen C1* closely match the experimental data, with small errors, as shown in Fig. 11a. Note that a peak base moment (4278*kip-ft.* (5800*kN-m*)) at 2% horizontal drift of the wall was recorded for the test results of *Specimen C1*, which is believed to be an outlier due to a glitch during the test, as the force readings in the horizontal actuators at that point were observed to be abnormally high when compared to prior and subsequent cycles [25]. Therefore, the base moment in the next excursion (i.e., at 3% drift) was taken to be the maximum positive base moment. With that, the maximum positive base moment of 3619*kip-ft.* (4907*kN-m*) was matched within 3.84% when comparing test result with those from analysis using the OpenSees model. In addition, the rotation at maximum positive base moment (0.0216 *rad*), corresponding to when the specimen was displaced to 3% drift, matched with a maximum difference of 5.47%. The maximum negative base moment (2504*kip-ft.* (3395*kN-m*)) was reached at 2.7% drift and the OpenSees result at that point matched within 2.76%. The rotation corresponding to the maximum negative base moment (−0.0141 *rad*) also had a good agreement, with differences remaining within 9%. A relatively good match was also obtained at the maximum rotation, with differences of 18% and 6% in the positive and negative moment values at the maximum rotations in their corresponding directions, and of 2.15% and 2.11% for the maximum positive and negative rotations, respectively.

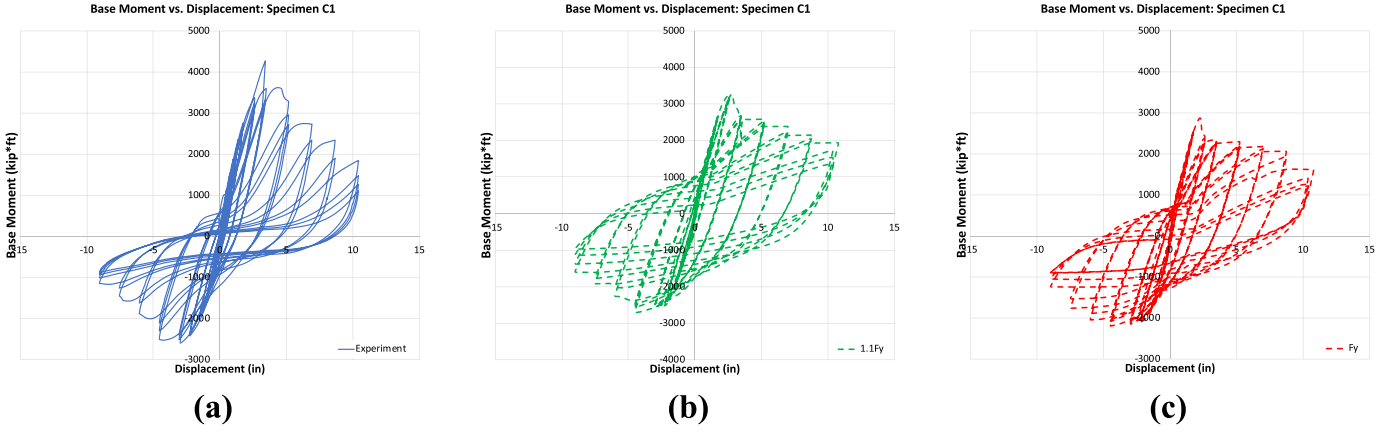

Fig. 13. Base moment versus displacement plots for Specimen C1: (a) experimental results; (b) analytical results for a yield stress of $1.1f_y$; (c) analytical results for a yield stress of $1.0f_y$ (Note: 1 in. = 25.4 mm; 1kip-ft = 1.36 kN-m).

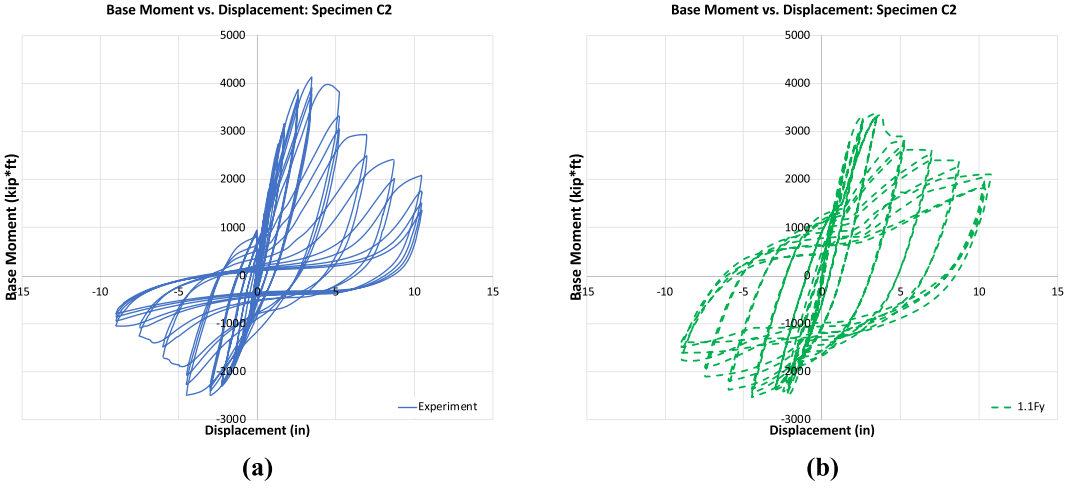

Fig. 14. Base moment versus displacement plots for Specimen C2: (a) experimental results; (b) analytical results for a yield stress of $1.1F_y$ (Note: 1 in. = 25.4 mm; 1kip-ft = 1.36 kN-m).

For *Specimen C2*, the difference between the experimental and OpenSees results in maximum positive and negative base moments increased to 10.5% and 5.02% (Fig. 11b), respectively. For the rotations at the maximum positive (0.01129 *rad*) and negative moments (−0.014 *rad*), the difference was greater than for *Specimen C1*, but still good, at 19% and 15%, respectively. However, a relatively better match was obtained for the maximum rotations, with differences of 1.1% and 0.54% in the positive and negative directions, respectively. Recall that the objective of the above calibration exercise was to select a single set of fatigue and buckling parameters that allowed matching as best as possible all of the test data of C-Shaped C-PSW/CF walls. Evidently, as mentioned earlier, slightly different values of parameters would have been obtained if the objective instead was to best match each of the test data individually. Note that the model replicated the pinching and progressive strength degradation well, which was one of the main objectives.

4.2.2. Distributed plasticity model with effective stress-strain curve approach

The C-shaped walls were similarly modelled using a fiber-based model with effective stress-strain material properties. The same effective stress-strain curves derived for the planar walls were implemented for the C-shaped walls. These effective stress-strain curves were presented in Fig. 5. An additional material model was applied to the corner sections as indicated in Fig. 12. The concrete in this box section was assigned a higher residual capacity due to the high level of steel reinforcement in this area.

The same OpenSees materials were used to model the C-shape wall behavior including *Reinforcing Steel* for the steel components of the walls and *Concrete02* for the concrete components. Properties from material testing were used to define f_y, f_u, and f'_c. The remainder of the backbone curve was defined to match closely the effective stress-strain curves. The steel and concrete material properties are reported in Tables 5 and 6, respectively.

Displacement-based nonlinear elements were used to model the plastic hinge region and elastic elements were used for the rest of the height. The length of the plastic hinge was half the length of the wall (50 *in.* (1270 *mm*)). This approach follows the distribution outlined in Fig. 3. Unlike the previous approach, the axial load set up was not directly modelled but instead, the axial load was applied through the center of the section and only the moment-top displacement response compared to the experimental data.

Base moment versus displacement comparisons for all specimens are plotted in Figs. 13 and 14. For Specimen C1 (Fig. 13), modeling results are reported considering a yield stress of $1.0f_y$ and $1.1f_y$. For Specimen C2, the analysis results from the model considering a steel yield stress of $1.1f_y$ are reported. As previously discussed, the OpenSees material model used for the steel material cannot have different compression and tension yield stresses as desired to match the effective stress-strain curves. Instead, two unique cases for a yield stress of $1.0f_y$ and $1.1f_y$ were considered to better understand the effect of the increase in yield stress. These curves show a good match between the initial stiffness, load at yield, unloading behavior, and residual capacity. The model is conservative for ultimate strength and predicted less pinching then observed in the experimental data. Nevertheless, the envelope behavior and overall cyclic behavior match well the experimental behavior, especially when considering a yield stress of $1.1f_y$.

Note that in the distributed plasticity modeling approach, coupon tests and unconfined concrete crushing tests were used to model the behavior of the walls. In other approach, however, results from benchmarked 3D finite element models were used to develop effective stress-strain curves that implicitly accounted for the effects of yielding, local buckling, and biaxial stresses on behavior [22,23]. Therefore, as a result, two different set of buckling parameters were considered to capture the behavior.

5. Summary and conclusion

Numerical models that have demonstrated their ability to replicate the hysteretic behavior of Composite Plate Shear Walls-Concrete Filled (C-PSW/CF) are needed in studies and projects for which non-linear inelastic analysis of is required. Here, non-linear models that can serve for this purpose have been identified and validated against experimental results for C-PSW/CF, while calibrating the parameters of these models to best capture the complete hysteretic behavior, including for stiffness and strength degradation due to buckling and fracture due to low-cycle fatigue. This goal is accomplished considering two different modeling approaches. For the first approach, walls were modelled using a fiber model using physical material models able to capture the effects of concrete cracking, steel yielding, local buckling, concrete crushing, and steel inelastic behavior up to fracture due to cumulative plastic strains and low cycle fatigue, with the defining parameters of these models empirically calibrated. For the second approach, the wall was modelled using a fiber model with effective stress-strain relationships assigned based on results of 3D finite element analysis that implicitly accounted for the effects of steel local buckling, yielding and fracture and concrete cracking, crushing and confinement. For both sets of models, the resulting models allowed to match both the experimentally-obtained force-displacement and moment-rotation hysteretic curves, including full stiffness and strength degradation due to buckling, fracture, and other non-linear behavior. The resulting knowledge on the value of the various parameters in such models can be used to perform nonlinear inelastic pushover analysis, cyclic analysis, and seismic time history analysis of C-PSW/CF systems in future studies. The information presented here can also serve as a basis for future developments to further enhance knowledge on the seismic behavior of C-PSW/CF.

Declaration of Competing Interest

The authors declare that they have no known competing financial interests or personal relationships that could have appeared to influence the work reported in this paper.

Acknowledgments

This research was conducted with support from the Charles Pankow Foundation (CPF) and the American Institute of Steel Construction (AISC), through CPF research grant #05-17 awarded to Michel Bruneau, from University at Buffalo, and Amit H. Varma, from Purdue University. However, any opinions, findings, conclusions, and recommendations presented here are those of the authors and do not necessarily reflect the views of the sponsor.

References

[1] Y. Alzeni, M. Bruneau, Cyclic Inelastic Behavior Of Concrete Filled Sandwich Panel Walls Subjected To In-plane Flexure, Technical Rep. MCEER 14-009 MCEER The State University of New York at Buffalo, 2014.
[2] K. Zhang, A.H. Varma, S.R. Malushte, S. Gallocher, Effect of shear connectors on local buckling and composite action in steel concrete composite walls, Nucl. Eng. Des. 269 (2014) 231–239.
[3] H. Bowerman, J.C. Chapman, Bi-steel steel-concrete-steel sandwich construction, Compos. Construct. Steel Concr. IV (2002) 656–667.
[4] J. Pryer, H. Bowerman, The development and use of British steel bi-steel, Proc., The Eighth International Offshore and Polar Engineering Conference, International Society of Offshore and Polar Engineers, 1998.
[5] ENR, Speed Core Research Tunes System, Engineering News-Records, 2020 , Retrieved from: https://www.enr.com/articles/48820-speed-core-research-tunes-system.
[6] ENR, Rainier Square Erector Says Speed Core Could Rise Even Faster, Engineering News-Records, 2020 , Retrieved from: https://www.enr.com/articles/48817-rainier-square-erector-says-speed-core-could-rise-even-faster.
[7] MSC, 850-FT-tall rainier square tower tops out in only 10 months, Modern Steel Construction, 2019 , Retrieved from: https://www.aisc.org/modernsteel/news/2019/august/rainier-square-tower-tops-out-at-850-ft-in-under-10-months/.

[8] M. Broberg, S. Shafaei, J. Seo, E. Kizilarslan, R. Klemencic, A.H. Varma, M. Bruneau, Capacity design of coupled composite plate shear walls – concrete filled (CC-PSW/CF), Journal of Structural Engineering (2020) In preparation.
[9] FEMA, NEHRP Recommended Seismic Provisions for New Buildings and Other Structures (FEMA P-2082-1). Volume I: Part 1 Provisions, Part 2 Commentary, Building Seismic Safety Council of the National Institute of Building Science, Washington D. C, 2020 FEMA P-2082-1.
[10] M. Bruneau, A.H. Varma, E. Kizilarslan, M. Broberg, S. Shafaei, J. Seo, R-factors for coupled composite plate shear walls /concrete filled (CC-PSW/CF), CFP Grant # 05-17, Charles Pankow Foundation, McLean, Virginia, 2019, 419 pp, Accessed from: R-factor report for CC-PSW/CF.
[11] E. Kizilarslan, M. Broberg, S. Shafaei, A.H. Varma, M. Bruneau, Seismic design coefficients and factors for coupled composite plate shear walls/concrete-filled (CC-PSW/CF), Eng. Struct. (2021) https://doi.org/10.1016/j.engstruct.2021.112766 Forthcomig.
[12] S.K. Kunnath, Y. Heo, J.F. Mohle, Nonlinear uniaxial material model for reinforcing steel bars, J. Struct. Eng. 135 (4) (2009) 335.
[13] F. McKenna, S. Mazzoni, G. Fenves, Open System for Earthquake Engineering Simulation (OpenSees) Software Version 2.2. 5, University of California, Berkeley, CA, 2016 , Available from http://opensees.berkeley.edu.
[14] A.M. Kanvinde, Methods to evaluate the dynamic stability of structures-shake table tests and nonlinear dynamic analyses, Proc., EERI Paper Competition, 2003 , (Winner. Proceedings of the EERI Meeting, Portland).
[15] D. Lignos, Sidesway Collapse of Deteriorating Structural Systems Under Seismic Excitations, Doctoral dissertation Stanford University, 2008.
[16] J.E. Rodgers, S.A. Mahin, Effects of connection fractures on global behavior of steel moment frames subjected to earthquakes, J. Struct. Eng. 132 (1) (2006) 78–88.
[17] FEMA, FEMA P695: Quantification of Building Seismic Performance Factors, Applied Technology Council. Federal Emergency Management Agency, 2009.
[18] G. Chang, J.B. Mander, Seismic Energy Based Fatigue Damage Analysis of Bridge Columns: Part 1-evaluation of Seismic Capacity, Technical Rep. MCEER 94-0006 MCEER The State University of New York at Buffalo, 1994.
[19] M. Hisham, M. Yassin, Nonlinear Analysis of Prestressed Concrete Structures under Monotonic and Cycling Loads, University of California, Berkeley, 1994.
[20] K. Susantha, H. Ge, T. Usami, Uniaxial stress–strain relationship of concrete confined by various shaped steel tubes, Eng. Struct. 23 (10) (2001) 1331–1347.
[21] ACI, Building Code Requirements for Structural Concrete (ACI 318-19) and Commentary, American Concrete Institute, 2019.
[22] S. Shafaei, A.H. Varma, M. Broberg, R. Klemencic, Modeling the cyclic behavior of composite plate shear walls / concrete filled (C-PSW/CF), Journal of Constructional Steel Research (2021) https://doi.org/10.1016/j.jcsr.2021.106810 In this issue.
[23] S. Shafaei, A.H. Varma, J. Seo, R. Klemencic, Cyclic lateral loading behavior of concrete filled composite plate shear walls, J. Struct. Eng. (2021) https://doi.org/10.1061/(ASCE)ST.1943-541X.0003091 ASCE, Forthcomig.
[24] Z. Tao, Z.-B. Wang, Q. Yu, Finite element modelling of concrete-filled steel stub columns under axial compression, J. Constr. Steel Res. 89 (2013) 121–131.
[25] H. Kenarangi, E. Kizilarslan, M. Bruneau, Cyclic behavior of c-shaped composite plate shear walls–concrete filled, Eng. Struct. 226 (2020) 111306.
[26] Y. Alzeni, M. Bruneau, In-plane cyclic testing of concrete-filled sandwich steel panel walls with and without boundary elements, Journal of Structural Engineering 143 (9) (2017) 04017115.